



# City Research Online

## City St George's, University of London

**Citation:** Morar, N., Holtham, N., Hackel, L., Davami, K., Sharma, M., DeWald, A. & Roy, R. (2023). Effects of high-energy laser peening followed by pre-hot corrosion on stress relaxation, microhardness, and fatigue life and strength of single-crystal nickel CMSX-4® superalloy. *The International Journal of Advanced Manufacturing Technology*, 126(11-12), pp. 4893-4912. doi: 10.1007/s00170-023-11358-5

This is the published version of the paper.

This version of the publication may differ from the final published version. To cite this item please consult the publisher's version.

**Permanent repository link:** <https://openaccess.city.ac.uk/id/eprint/30277/>

**Link to published version:** <https://doi.org/10.1007/s00170-023-11358-5>

**Copyright and Reuse:** Copyright and Moral Rights remain with the author(s) and/or copyright holders. Copies of full items can be used for personal research or study, educational, or not-for-profit purposes without prior permission or charge, unless otherwise indicated, provided that the authors, title and full bibliographic details are credited, a hyperlink and/or URL is given for the original metadata page and the content is not changed in any way. For full details of reuse please refer to [City Research Online policy](#).



# Effects of high-energy laser peening followed by pre-hot corrosion on stress relaxation, microhardness, and fatigue life and strength of single-crystal nickel CMSX-4<sup>®</sup> superalloy

Nicolau Iralal Morar<sup>1</sup> · Noah Holtham<sup>2</sup> · Lloyd Hackel<sup>3</sup> · Keivan Davami<sup>2</sup> · Montu Sharma<sup>3</sup> · Adrian DeWald<sup>4</sup> · Rajkumar Roy<sup>1</sup>

Received: 28 December 2022 / Accepted: 30 March 2023

© The Author(s) 2023

## Abstract

This study investigated the stress relaxation and fatigue life and strength of laser-peened single-crystal nickel superalloy specimens compared to unpeened and shot-peened specimens following hot corrosion exposure and then fatigue testing. The specimens were treated by conventional laser peening and a new cyclic laser peening plus thermal microstructure engineering process. The latter treatment supports the benefit of a unique process involving application of layers of laser peening using high energy with large footprint spots combined with interspersed cyclic annealing. Stress measurements by slitting showed the plastic penetration depth of laser peening exceeded shot peening by a factor of 24. Unpeened and peened specimens were exposed to sulphate corrosives at 700 °C for 300 h and then fatigue tested. Tests of five non-laser-peened specimens all failed in low-cycle fatigue regime, whereas three identically tested laser-peened specimens all achieved multi-million-cycle runout without failure, indicating fully consistent large benefit for life by laser peening. Additional tests also showed fatigue strength improvement of 2:1 by laser peening. Residual stress measurements post hot-corrosion exposure and fatigue testing showed notable 5 mm depth retention of residual eigenstress in a laser-peened specimen.

**Keywords** Laser peening · Fatigue strength · Stress relaxation · Corrosion · Ni-based superalloy

## 1 Introduction

Single crystal (SC) CMSX-4<sup>®</sup> nickel-based superalloy is extensively used in aircraft and power generation gas turbine applications for its high-temperature and creep resistance [1]. With increasing demand to maximise energy efficiency, operating temperatures need to be as high as possible, and consequently, next-generation gas turbines need nickel

superalloy components with enhanced oxidation and stress corrosion cracking resistance to offer longer and more reliable service lifetime. This can be achieved using mechanical surface treatments such as shot peening (SP) and laser peening (LP). The latter surface treatment utilises laser energy which provides high irradiance and large multi-millimetre scale footprints on the target surfaces to impart sufficient pressure into the sub-surface layers to create local plastic deformation and the subsequent formation of deep compressive residual stresses (CRS) and work-hardened sub-surface layers [2, 3]. It is established that both deeply penetrating CRS and a strong work-hardened surface layer retard crack initiation and growth, enabling fatigue life extension of metallic components and structures [4].

In recent years, high-energy LP has received much interest as a method for the surface engineering of nickel-based superalloys due to its deep level of induced compressive stresses, flexibility, high productivity, and environmentally friendly operation. The compressive residual stresses from LP significantly enhance the strength of the material against surface-initiated failures. There have been a number

✉ Nicolau Iralal Morar  
nicolau.morar@city.ac.uk

✉ Lloyd Hackel  
Lloyd.Hackel@cwst.com

<sup>1</sup> Department of Engineering, City, University of London, Northampton Square, London EC1V 0HB, UK

<sup>2</sup> Department of Mechanical Engineering, University of Alabama, Tuscaloosa, AL 35487, USA

<sup>3</sup> Curtiss Wright Surface Technologies - Metal Improvement Company, Livermore, CA, USA

<sup>4</sup> Hill Engineering, LLC, Clearfield, UT, USA

of studies investigating the effects of LP on SC Ni-based superalloy stresses and microstructures [5–11]. LP has been shown to produce a large number of dislocation structures without compromising the integrity of the strengthening mechanisms of the superalloy mainly attributed to  $\gamma$  and  $\gamma'$  phases. Moreover, a high-density of dislocations caused by the LP-induced plastic deformation increased the microhardness of the surface and subsurface regions of the SC Ni-based superalloys that were studied. However, when exposed to higher temperatures ( $> 400$  °C), these treated superalloys undergo a stress relaxation stage, potentially compromising their fatigue resistance.

A limited number of studies have investigated the effects of LP on SC Ni-based superalloys in fatigue loading conditions and hot corrosive environments [12–15]. The failure of the structure due to hot corrosion and fatigue is caused by elevated temperatures, cyclic mechanical loading, combustion gases, and airborne contaminants [16, 17]. Therefore, thermal microstructural stability and surface enhancement are critical to Ni-based superalloys in order to improve their resistance to surface cracking mechanisms such as thermal fatigue and stress corrosion cracking damages in extreme environments. Geng et al. [12] studied the hot corrosion behaviour of a Ni-based SC superalloy treated by laser peening against 75 wt.%  $\text{Na}_2\text{SO}_4$  + 25 wt.%  $\text{NaCl}$  molten salts at 750°. It was shown that the LP process improved the hot corrosion resistance of the SC superalloy. This was attributed to the LP-induced high-density dislocations in the  $\gamma$  phase that encouraged and facilitated the outward diffusion of Cr. This led to the formation of a Cr-rich oxide film. Simultaneously, a lower density of dislocations in the strengthening  $\gamma'$  phase further assisted with the outward diffusion of Al to form a ceramic,  $\text{Al}_2\text{O}_3$ , layer. It was shown that the resultant oxide films that act as a “shield” prevented the inward diffusion of corrosive elements such as S and improved the corrosion behaviour. Tang et al. [13] implemented a modified LP process to evaluate its effect on the hot corrosion behaviour of SC Ni-based superalloy. Results showed enhanced hot corrosion resistance of the treated specimens, and this was attributed to stable dislocation structures; however, the exact mechanism was not clear and needed further research.

Also, fatigue behaviour of laser-peened SC Ni-based superalloys was investigated by Tang et al. [8] and Lu et al. [7]. It was found that the formation of dislocation networks and superlattice intrinsic stacking fault (SISF) in the  $\gamma$  and  $\gamma'$  phases by LP treatments hindered the crack growth and benefited fatigue life of superalloy specimens tested. These studies [5–8] suggest that LP treatments can be used to enhance surface and sub-surface properties of SC Ni-based superalloys not only by inducing compressive residual stresses and work hardening but also through generating highly stable dislocation structure and their interactions with precipitates.

The latter facilitates the reduction of stress relaxation under cyclic and thermal-loading conditions [18].

The majority of the aforementioned studies were conducted using laser energies in the sub-joule range, meaning that a small spot size had to be used to achieve the desired irradiance. Small spot sizes reduce the depth of plastic penetration of the pressure wave by approximately the beam diameter (diagonal for a square beam) and that directly impacts the effectiveness of the peening process against surface-initiated failures. In spite of these studies, high-energy LP of SC Ni-based superalloys has not been fully validated for industry use due to a limited understanding of stress relaxation and fatigue behaviour under high-temperature corrosive environments.

In this study we focus on improving fatigue strength and high-temperature corrosion resistance of CMSX-4® superalloy through laser peening plus thermal microstructure engineering (LP + TME), that has not been investigated before [19]. This treatment supports the benefit of a unique process involving application of layers of laser peening using high energy with large footprint spots combined with interspersed cyclic annealing. LP + TME has shown to provide higher CRS than LP, and the relaxation of stresses at elevated temperature is significantly mitigated [20–22], benefiting fatigue life extension of the alloy. This thermal stability is attributed to the interaction of strengthening precipitates with the dislocation structures generated by LP + TME. These precipitates act as pinning points on the dislocations and restrict their movement [23]. Therefore, high-energy LP + TME of single-crystal CMSX-4® superalloy is a promising surface engineering technique for extreme environment such the one in turbine blade root applications.

## 2 Experimental setup

### 2.1 Material and specimens

In the present study, the target material is a second-generation heat-treated single-crystal nickel-based CMSX-4® superalloy. The material was provided by a UK aerospace manufacturer and supplied in cylinders of 130 mm length, 23 mm diameter with [001] crystallographic orientation lying along the length of the bar. The material chemical composition is in weight %: Cr 6.5, Co 9.0, Mo 0.6, Al 5.6, Ti 1.0, Ta 6.5, W 6.0, Hf 0.1, Re 3.0, and Ni balance [24].

The heat-treated CMSX-4 bars were cut by wire electrical discharge machining (wire-EDM) and post-processed to remove machining remnants to produce two sets of specimens: first, a set of disc specimens for initial screening trials to down-select optimal laser peening conditions for corrosion and fatigue strength testing. Disc specimens were used for microstructural characterisation and residual stress

measurements both before and after thermal exposure. Secondly, a set of semi-circular notch specimens were machined to assess fatigue strength of laser-peened and unpeened CMSX-4 superalloy, as well as shot peened for comparison purpose. Eleven disc specimens were produced with three different laser-peening conditions and each disc has 23 mm diameter and 10 mm thickness, as shown in Fig. 1. For each LP condition, a set of 3 specimens were peened under the same conditions to validate findings.

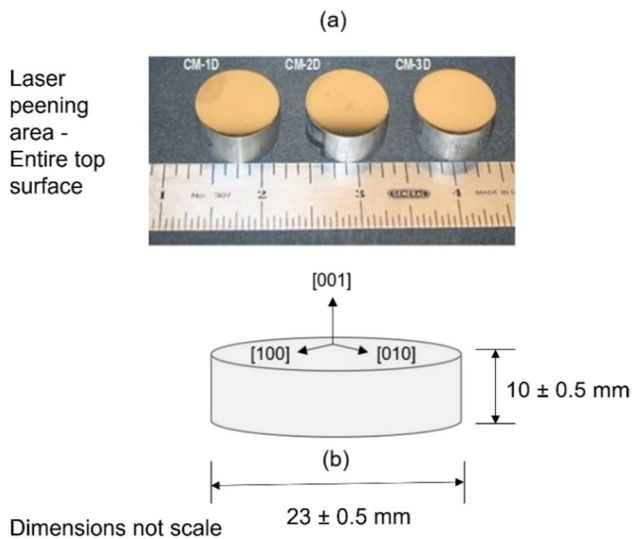
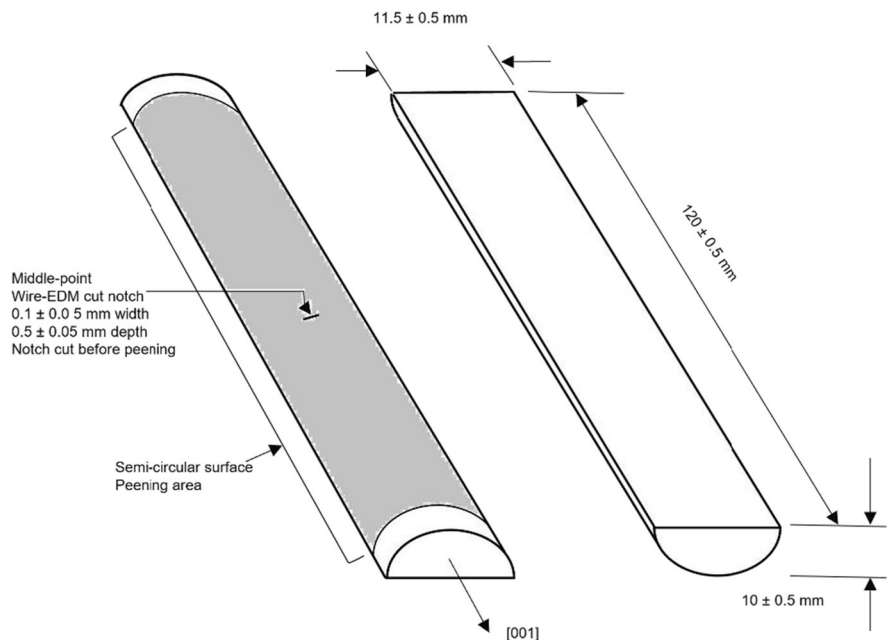


**Fig. 1** Disc specimens of CMSX-4® superalloy for initial laser peening treatment (a) and schematic of disc sample illustrating dimensions and crystallographic orientations (b). The primary and secondary crystallography orientations were determined by the back-reflection Laue method

**Fig. 2** Schematic of semi-circular notch bending fatigue specimen. Dimensions not to scale



For fatigue testing, four available CMSX-4® single-crystal cylinder rods were machined into eight semi-circular 4-point bend test specimens by first cutting off each end, making squared up cylinders of 120 mm length. The cylinders were then cut in half lengthwise by wire-EDM, creating semi-circular sections and finally each was specimen precisely machined to  $11.0 \pm 0.5$  mm thickness. Prior to peening, a notch of 1 mm width and 0.5 mm depth was wire-EDM cut at mid-point into the top arc of each specimen. This notch created a consistent failure point and simulated a local stress riser in an operational turbine component as would be expected, for example, at a blade root section by a corrosion pit or stress corrosion-assisted micro-cracking. A  $K_t$  factor of 5.3 was calculated for this notch geometry by means of finite element analysis [25] and verified under elastic-only load with strain gauges applied to a test specimen. Moreover, the fatigue specimen geometry has been validated by industrial partners, and the processing parameters and resting conditions are described in Sect. 2.5. The peening on the disc specimens covered the entire surface area, while on the fatigue test specimens, the peening coverage extended to the circular surface area including the full gauge length (see Fig. 2).

## 2.2 Laser peening

The laser peening of all samples was performed at the Metal Improvement Company Curtis-Wright Surface Technologies facility (in Livermore, USA) using a 20 J/pulse Nd-glass laser employing a Q-switched Nd:YLF master oscillator and phase-conjugated power amplifier operating at 1053  $\mu\text{m}$  wavelength. Prior to laser peening, the surface of

each sample was ground using SiC papers about 0.2 mm to remove remnants of wire-EDM recast on both surfaces and followed by an ultrasonic cleaning process. The selected LP parameters are shown in Table 1. Laser irradiances ranging from 4 to 10 GW/cm<sup>2</sup> were used in the initial laser peening and stress evaluations, and then an irradiance of 7 GW/cm<sup>2</sup> was chosen for treatment of fatigue test specimens with the purpose of maximising compressive residual stress. The irradiance range used was based on matching the reported yield stress [24] to the calculated pressure generated by the laser peening of materials previously peened and evaluated [21], but importantly matched to the stiffness (moment of inertia) of the test specimen so as to maximise depth and intensity of residual stress by limiting specimen strain.

Laser-peening parameters used for actual components would depend on component geometry, specifically stiffness, as it relates to component ability to retain stress. Laser spots were square and overlapped in both dimensions by 3%, equating to 100 microns, with the overlap calibrated across the pattern width. Deionised water of 15 M $\Omega$  minimum resistance and about 1 mm thickness was flowed over each spot area with the tamping fluid flow rate sufficient to re-establish laminar flow for each individual laser pulse. Three or four layers of coverage were applied to each laser-peened area with no ablative layer used over the metal in the process. A schematic of the laser peening process is illustrated in Fig. 3.

A shorthand notation of LP processing of samples used in this study, for example, LP or LP+TME X–Y–Z, has been defined for the laser-peening treatments. The first number represents the irradiance (GW/cm<sup>2</sup>), the second number the pulse duration (ns), and the third, the number of laser beam coverage layers. The designation TME (thermal microstructural engineering) is given to a newly developed process by Curtiss-Wright in which cyclically a layer of laser peening was applied, the specimen annealed, and then subsequent peening and annealing performed with this process ending with a final peening. Finally, the recast layer of about 5  $\mu$ m thickness generated by peening without an ablative layer is removed by fine polishing.

### 2.3 Surface topology

The surface topography of the LP samples was characterised by an optical 3-D profiler (Talysurf 6000 CCI). Table 2 shows

**Table 1** Laser peening process parameters

| Wavelength ( $\mu$ m) | Irradiance (GW/cm <sup>2</sup> ) | Pulse duration (ns) | Area of laser spot (mm <sup>2</sup> ) | Overlapping rate (%) |
|-----------------------|----------------------------------|---------------------|---------------------------------------|----------------------|
| 1053                  | 4, 7, and 10                     | 18                  | 12.7                                  | 3                    |

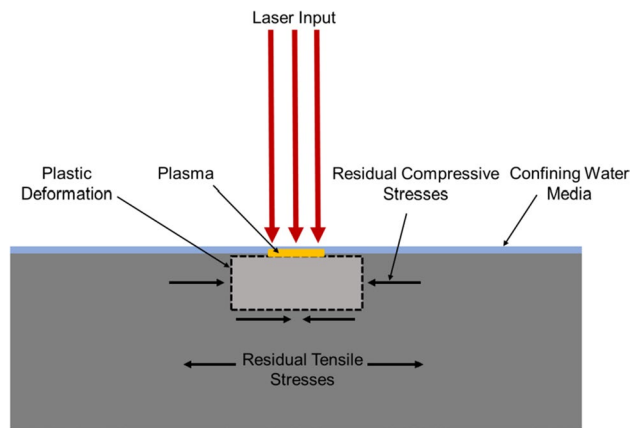


**Fig. 3** Illustration of a laser peening setup shows a laser beam incident on a component's surface covered with deionised water. The laser light passes unabsorbed through the water, striking and heating a plasma. The laser irradiance is adjusted so that the plasma creates a pressure about 1 to 2 times greater than the dynamic yield strength of the material. The plasma pressure propagates into the material plastically yielding and creating resultant stress and strain depending on the geometric resistance of the component [26]

the parameters used for carrying out the surface roughness (Ra) characterisation. Three arbitrary points were considered on each disc specimen for accuracy, and the mean value was reported. Only three LP disc specimens, viz., LP 4–18-3, LP 7–18-3, and LP 10–18-3, were subjected to roughness measurements before and after 50 h of thermal exposure at 700 °C. Also, a bare untreated CMSX-4® sample was analysed for the comparison.

### 2.4 Microscopy and microhardness

The cross-section microstructure of LP samples was characterised by scanning electron microscopy (SEM, using a Philips Scanning Electron Microscope XL30 S FEG and a Thermo Scientific Apreo FE-SEM), using secondary electron imaging (SEM SE). The cross-sectioned samples were prepared using standard metallographic procedures and then electro-chemically etched using 10% phosphoric acid, 90% deionised water with 2.4 mV applied for 20 s. Lamellas were extracted using a focussed ion beam (FIB, TESCAN LYRA FIB-FESEM) milling method at a distance of 150  $\mu$ m from the treated surface. A transmission electron microscope (TEM, FEI Tecnai F-20) was used to generate the highest-resolution images.

To evaluate the magnitude of work hardening due to laser peening, preliminary microhardness profiles were measured

**Table 2** Talysurf 6000 CCI parameters

| Focal point (mm) | Magnification | Aperture ( $\mu$ m <sup>2</sup> ) | Filter |
|------------------|---------------|-----------------------------------|--------|
| 3.4              | ×50           | 360                               | Red    |

on the face perpendicular to the LP surface which is roughly parallel to the [010] plane using a Clemex Vickers Microhardness Tester (Clemex Technologies Inc., Canada) with an indentation load of 300 gf (~3 N) and holding time of 10 s. To minimise error, all tests were conducted in triplicates and their values were taken as the preliminary results. Further experimental tests are ongoing on other laser-peening conditions.

### 2.5 Residual stress measurements

In this study the residual stress measurements were made using the crack compliance slitting technique introduced by [21, 25] and presented in eigenstresses. The “slitting” technique has been used to measure residual stresses of different surface treated materials [27–30]. The slitting technique involves a global fitting to strain differences made at progressive cut depths as measured by a strain gauge positioned on the opposite side of the cut surface. A stress distribution is obtained by a polynomial best fit of the back-side measurements to the model and conversion via the material elastic modulus. In slitting, measurements of strain releases from the gauge on the back side of the sample are recorded as wire-EDM cuts; on the order of 100 µm steps are made in the depth of the sample. Strain release is measured as a function of depth [31]. A schematic diagram of the slitting technique procedure is shown in Fig. 4. The ability to measure stress through nearly the entire thickness of a sample is distinct feature of the slitting technique, especially for evaluating deep penetration processes like laser peening.

Extrapolating the thickness of the block to near infinity where the straining becomes infinitely small and stress release near zero, an estimate of the depth of plastic deformation generated by the laser peening is obtained as function of cutting depth. This is called the eigenstress. Eigenstrain and eigenstress, generated by use of the material modulus of elasticity, represent the actual plastic response of the material in a component to peening independent of its geometry [31]. Combining eigenstrain and the finite elements code, stress and strain generated in a material of arbitrary geometry can be computed as function of depth.

A polynomial least squares method is used to find the best fit of the measured strain changes to the model prediction

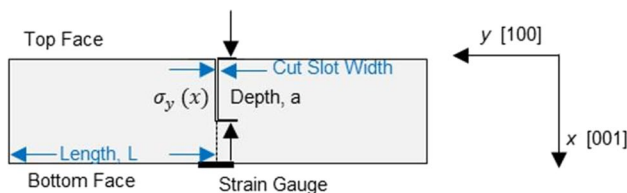


Fig. 4 Schematic laser peened with position of the crystallographic orientations in respect to cut/slitting direction

using different orders of polynomial fit. Polynomials of orders 3 to 6 are generally considered reasonable for simple geometries such as a rectangular block or a disc, as used in this work. It was assumed that the specimen was isotropic and responded in a linear elastic manner with Young's modulus ( $E_{[001]}$ ) 128 GPa and Poisson's ratio ( $\nu_{[001]}$ ) 0.38, which are typical values for CMSX-4 superalloy [24].

### 2.6 Fatigue testing

The fatigue testing was done on an Instron 1880 fatigue rig in 4-point bending configuration at  $R=0.1$  incorporating a wire-EDM notch of 500-micron depth which added a  $K_t$  factor of 5.3. The  $K_t$  factor was calculated using a finite element method (see Fig. 5). The notch gave a significant stress increase at specimen centre as would be the case for stress in a 3-point bending test. The chosen notch depth and thus  $K_t$  factor were guided by consideration of the geometry and subsequent in-service corrosion pits often generated in blade root (or platform) areas. The semi-circular specimens were utilised to maximise testing from a limited quantity of SC bars. The specific geometry, fabrication and peening coverage used on the specimens are shown in detail in Fig. 2. The stress calibration was performed in the same 4-point bending setup with specimens at a room temperature of  $22\text{ }^\circ\text{C} \pm 5.0\text{ }^\circ\text{C}$ . Sinusoidal cyclic loading was applied at 8 Hz with  $R=0.1$ .

Figure 6 shows the rig setup and the fatigue specimen loading configuration with the semi-circular side (tensile side under load) of the fatigue specimen oriented downward. To calibrate loading and calculate and confirm the model prediction of stress in the specimen, (neglecting the  $K_t$  increased stress in the notch or subsequent yielding under load), a strain gauge was attached to the centre of the flat bottom side of a specimen and strain values measured as the specimen were statically loaded in 4-point bending on the 90-kN load frame.

Prior to testing, six of the fatigue specimens were coated with one of two corrosive salts, sodium sulphate ( $\text{Na}_2\text{SO}_4$ ),

#### Notched Kt calculation

- Smax (unnotched): 30.80 ksi 212 MPa
- Notch diameter: 0.012"
- Notch depth: 0.012" (wire diameter) + 0.019685" (0.5 mm) = 0.031685
- Smax in notch: 163.2 ksi 1125 MPa
- Kt: 5.3

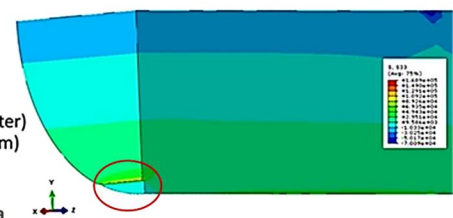


Fig. 5 Stress intensity factor modelling of slitted notch of semi-circular fatigue bending specimen by finite element analysis

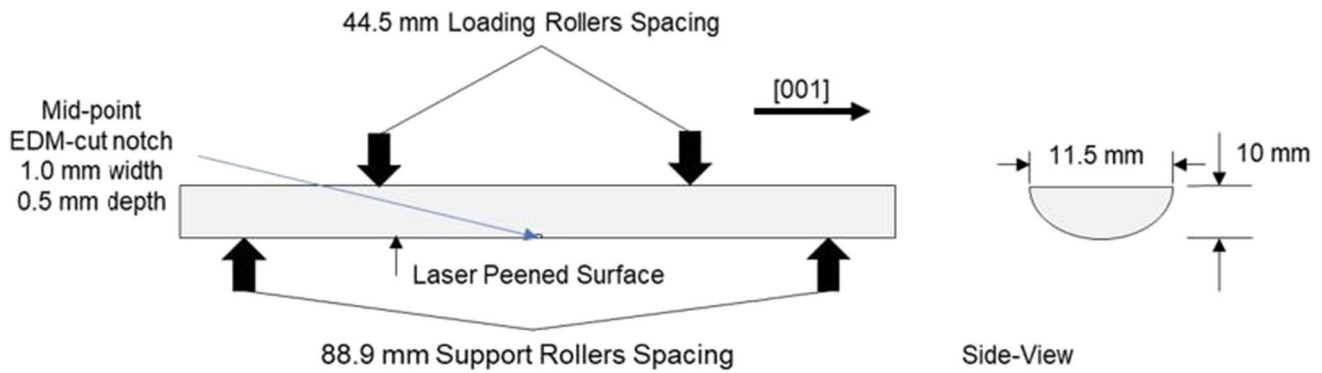


Fig. 6 Schematic of fatigue specimen and four-point bend test configuration

Table 3 Laser-peened specimens surface roughness

| Laser peening | Before thermal exposure | After thermal exposure |
|---------------|-------------------------|------------------------|
| Baseline      | 15.7 ± 3 nm             | -                      |
| LP 4–18–3     | 91.1 ± 9 nm             | 84.4 ± 2.3 nm          |
| LP 7–18–4     | 111.7 ± 9 nm            | 99.3 ± 4.7 nm          |
| LP 10–18–5    | 134.3 ± 10 nm           | 100.0 ± 4.3 nm         |

or potassium sulphate ( $K_2SO_4$ ), and then thermally pre-soaked in air at 700 °C for 300 h to mimic hot corrosion conditions. The salt deposition was applied on the arc surface area of the specimen with a salt flux target of 0.6 mg/cm<sup>2</sup>. Figure 6 shows the specimen design, the notch configuration, and gives the loading used to model and convert the applied loads to stresses in the specimens. A thousand to several hundred-thousand cycles was chosen as the low-cycle fatigue criterion and greater than one million cycles was set as the run-out condition. A failure criterion of 10% displacement compliance was used for the testing. Using the strain gauge for calibration, we report the actual stress loads applied to the specimens, not making elastic–plastic corrections for the  $K_t$  factor or stress redistribution in the notch.

### 3 Results and discussions

#### 3.1 Surface roughness

The average values of the surface roughness of all the specimens measured are shown in Table 3. The surface roughness of the LP specimens was measured inside the laser spot region. It was observed that the bare CMSX-4@ specimen showed a much smoother surface as expected, whereas the LP specimens showed an increase in roughness relative to the increase in power density, under the range of values tested. This change in surface topography is attributed to the magnitude of plasma formed on the surface and

overlap layers resulting from the repetition of high intensity LP treatment (from 4, 7, to 10 GW/cm<sup>2</sup>). This, in turn, creates deeper regions of plateaus and troughs on the surface of the material which make the surface rougher.

After thermal exposure at 700 °C for 50 h, the LP-treated specimens denoted as TE (thermally exposed) became much smoother, and the roughness slightly decreased (see Table 3). The high-temperature exposure leads to surface oxidation causing change in the surface roughness under conditions exposed and, hence, generating a homogeneous surface layer. Although, surface roughness of the LP + TME specimen was not measured, the findings here show that interspersed annealing cycles at 700 °C would yield lower roughness than standard LP treatment.

The analysis of surface topography after the LP treatment is also crucial as it facilitates the selection of optimal process variables as well as maintaining a good surface quality and hence material's fatigue life. In general, when the specimen is LPed at lower power densities, the compressive residual stresses generated are minimal and would not benefit the fatigue life of the peened material to a greater extent but provide a relatively smoother surface. On the other hand, at higher power densities, even though the roughness is increased substantially, the compressive residual stresses generated increase the material's fatigue life greatly. There are a number of post-processing techniques such as polishing, grit blasting, etc., that can be used to reduce the roughness of the material after LP. The main challenge regarding surface roughness is to make sure that the material being peened has sufficient residual stresses, while also not generating an excessively rough surface. Still, it must be considered that LP treatment has a very little effect on the roughness of the material when compared to other surface treatments such as SP.

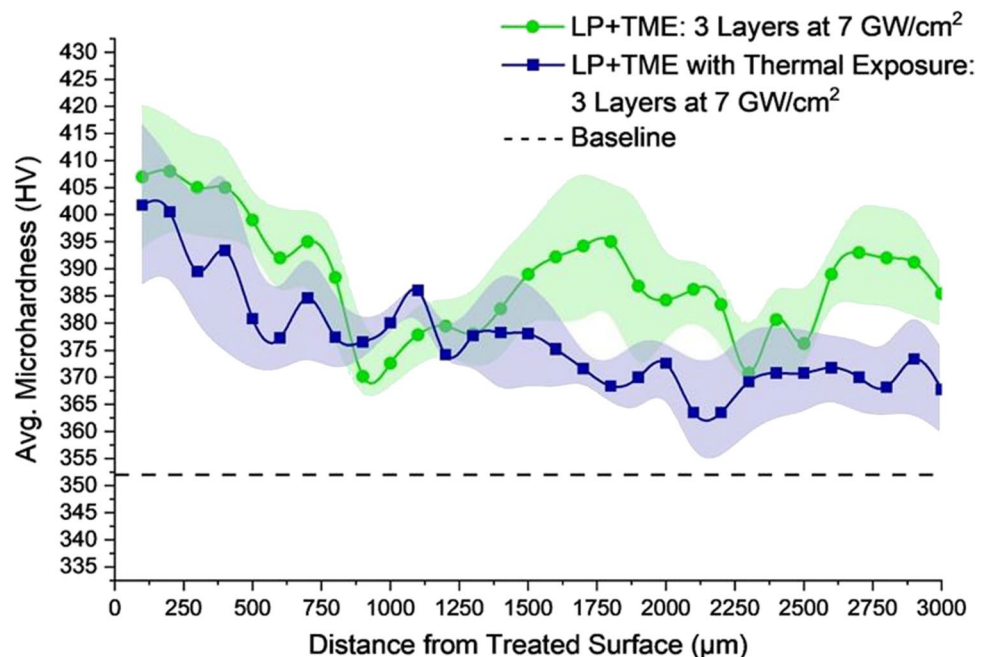
#### 3.2 Microhardness

Microhardness data was collected from all samples at regular intervals of depth from the LP + TME 7–18–3 surface and

plotted in Fig. 7. Baseline hardness measurements were taken on the same plane to account for error associated with the anisotropic material properties inherent to CMSX-4. In the LP+TME 7–18–3 condition, a 16% gain in surface microhardness (407 HV) over the baseline sample (352 HV) is observed. These results are expected as the 7 GW/cm<sup>2</sup> power density generates a pressure pulse equivalent to ~2 times the Hugoniot elastic limit (HEL) of CMSX-4. HEL is a material property which describes the transition from purely elastic to an elastic–plastic state under shock loading conditions, and peak values of plastic strain have been shown to occur between 2 and 2.5 times the HEL [32]. Thus, 7 GW/cm<sup>2</sup> generated maximum plastic strain at the surface and elastically deformed the surrounding material, generating a state of compressive residual stress. These residual stresses (in confluence with work hardening effects) led to a hardening of the treated surface up to a depth of ~3 mm (see Fig. 7). Following a 700 °C exposure for 300 h, the LP+TME 7–18–3–treated sample retained around 99% of its surface microhardness (402 HV) which is a testament to the stability of LP+TME-induced dislocation structures and their resistance to reorganisation. An additional point of note is that the microhardness measurements do not attenuate back to the baseline value and the maximum measured depth of 3 mm due to the residual stress which extend up to ~4 mm as will be discussed in Sect. 3.3.

To determine the correlation between mechanical properties and microstructure evolution, electron microscopy was conducted on all the specimens following thermal exposure to investigate the mechanisms behind the observed enhanced microhardness. Results are presented in the following section.

**Fig. 7** Microhardness distribution of the CMSX-4 laser-peened samples before and after thermal exposure at 700 °C



### 3.3 Microstructure

To better understand how LP+TME affects the microstructure of CMSX-4, SEM images were taken on a face perpendicular to the treated surface (Fig. 8a–d). Figure 8a shows a representative image of the microstructure prior to any surface treatment. The cuboidal nature of the  $\gamma'$  (dark grey) precipitates indicates a high degree of coherency with the surrounding  $\gamma$  matrix (light grey) in the as-cast condition. Following LP+TME at 7 GW/cm<sup>2</sup>, a distinct layer of resolidified material formed due to the rapid heating and cooling of the surface (Fig. 8b, c). This layer does not provide any strengthening and is typically removed prior to use. In this work though, the resolidified layer has been left intact to provide an accurate depiction of the surface and subsurface microstructure following LP+TME. The image processing software ImageJ was used to measure the area fraction of  $\gamma'$  precipitates, and there was found to be no change in the size, shape, and distribution of  $\gamma'$  phases following LP+TME as well as after exposure to 700 °C for 300 h (Fig. 8d). Table 3 shows small changes in area fraction are within the margin of error with this method ~8%. The results in Fig. 8 and Table 4 show that although the material has undergone intense plastic deformation from 3 layers of laser peening at ~2 times the Hugoniot elastic limit (HEL) of CMSX-4 as well as annealing heat treatments at 700 °C for 8 h, the morphology of the  $\gamma/\gamma'$  microstructure remains unchanged.

In the design of a post-processing technique which is meant to improve the structural characteristics of a material, it is of great importance to not degrade any pre-existing strengthening mechanisms. CMSX-4 is largely strengthened

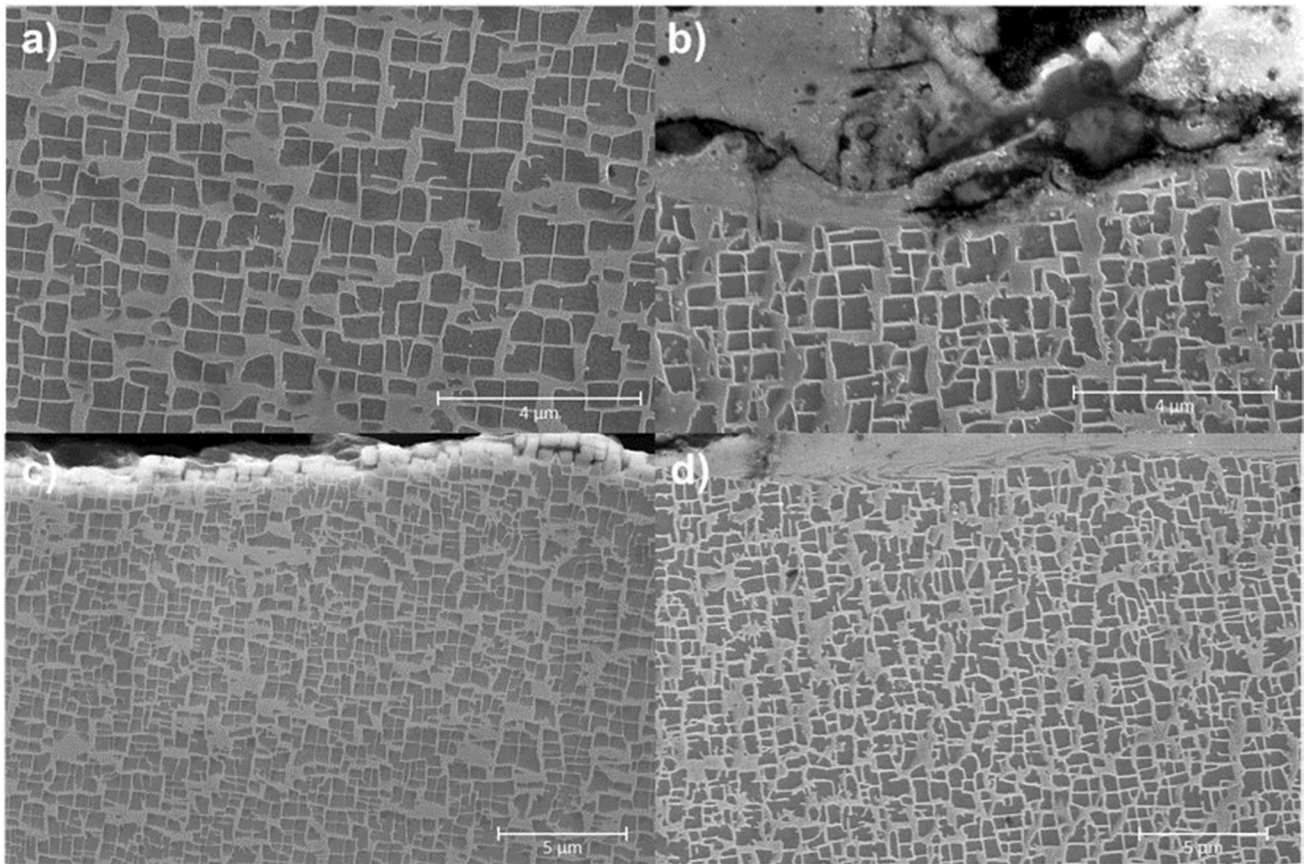


**Fig. 8** SEM micrographs of the CMSX-4 microstructure **a** prior to treatment, **b** treated surface following LP+TME, **c** following 7-18-3 LP+TME treatment, and **d** following 700 °C thermal exposure for 300 h

**Table 4** CMSX-4 fatigue test specimen identification and treatments

| No | SN    | Surface treatment | Salt deposition                 | Pre-soak        |
|----|-------|-------------------|---------------------------------|-----------------|
| 1  | RSC-1 | Shot peening      | Na <sub>2</sub> SO <sub>4</sub> | 300 h at 700 °C |
| 2  | RSC-2 | CMSX-4 baseline   | None                            | 300 h at 700 °C |
| 3  | RSC-3 | LP 7-18-4         | Na <sub>2</sub> SO <sub>4</sub> | 300 h at 700 °C |
| 4  | RSC-4 | LP+TME 7-18-4     | Na <sub>2</sub> SO <sub>4</sub> | 300 h at 700 °C |
| 5  | RSC-5 | Bare              | K <sub>2</sub> SO <sub>4</sub>  | 300 h at 700 °C |
| 6  | RSC-6 | LP+TME 7-18-4     | K <sub>2</sub> SO <sub>4</sub>  | 300 h at 700 °C |
| 7  | RSC-7 | Bare              | Na <sub>2</sub> SO <sub>4</sub> | 300 h at 700 °C |

by the L1<sub>2</sub>-ordered  $\gamma'$  phases precipitated within the disordered  $\gamma$  matrix (Fig. 8a). Though the phases are coherent, there is a degree of elastic misfit between them which creates stresses in the  $\gamma$  channels (compressive for negative misfit alloys such as CMSX-4) (Table 5). These misfit stresses also contribute to enhanced strength by inhibiting dislocation movement within the  $\gamma$  channels. Under intense thermo-mechanical loads, the  $\gamma'$  precipitates begin to take on a more rounded shape, which indicates a loss of coherency with the matrix and an overall weakening of the material.

**Table 5** Area fraction of  $\gamma'$  phases in LP+TME-treated CMSX-4@ before and after thermal exposure

| Distance from LP surface | Baseline | LP+TME 7-18-3 | LP+TME 7-18-3 w thermal exposure |
|--------------------------|----------|---------------|----------------------------------|
| 50 $\mu$ m               | 51%      | 55%           | 51%                              |
| > 5 mm                   | 51%      | 52%           | 53%                              |

Therefore, it is the goal of LP+TME, from a microstructural perspective, to create a thermally stable zone of plastic deformation which prevents the relaxation of residual stresses without degrading the coherency hardening effects and other strengthening mechanisms intrinsic to CMSX-4.

Further microstructural analysis of LP+TME-treated samples before and after thermal exposure was conducted using TEM (Fig. 9). A lamella was extracted from a region 150  $\mu$ m below the treated surface (lamellas taken any closer to the surface yielded difficult imaging conditions due to the intensity of plastic deformation) using FIB and was subsequently attached to a copper grid and thinned to a width of ~ 100 nm.

Several dislocation configurations were observed following LP+TME such as  $\gamma/\gamma'$  interfacial dislocations, curved dislocations lines, and dislocation shearing of the  $\gamma'$  phases which can be seen in Fig. 9a and 9b. A close-up view of a curved dislocation line is circled in Fig. 9b. The ordered nature of  $\gamma'$  precipitates necessitates the creation of an antiphase boundary as well as the passing of an additional dislocation to restore

the order, and thus, much more energy is needed for dislocations to shear through the  $\gamma'$  phase than the disordered  $\gamma$  phase. Consequently, during mechanical loading, dislocation pile up occurs at the phase boundaries until sufficient stress allows for the shearing mechanism to activate. These findings concur with a study conducted by [9] where the authors found precipitate shearing to be a dominant deformation mechanism

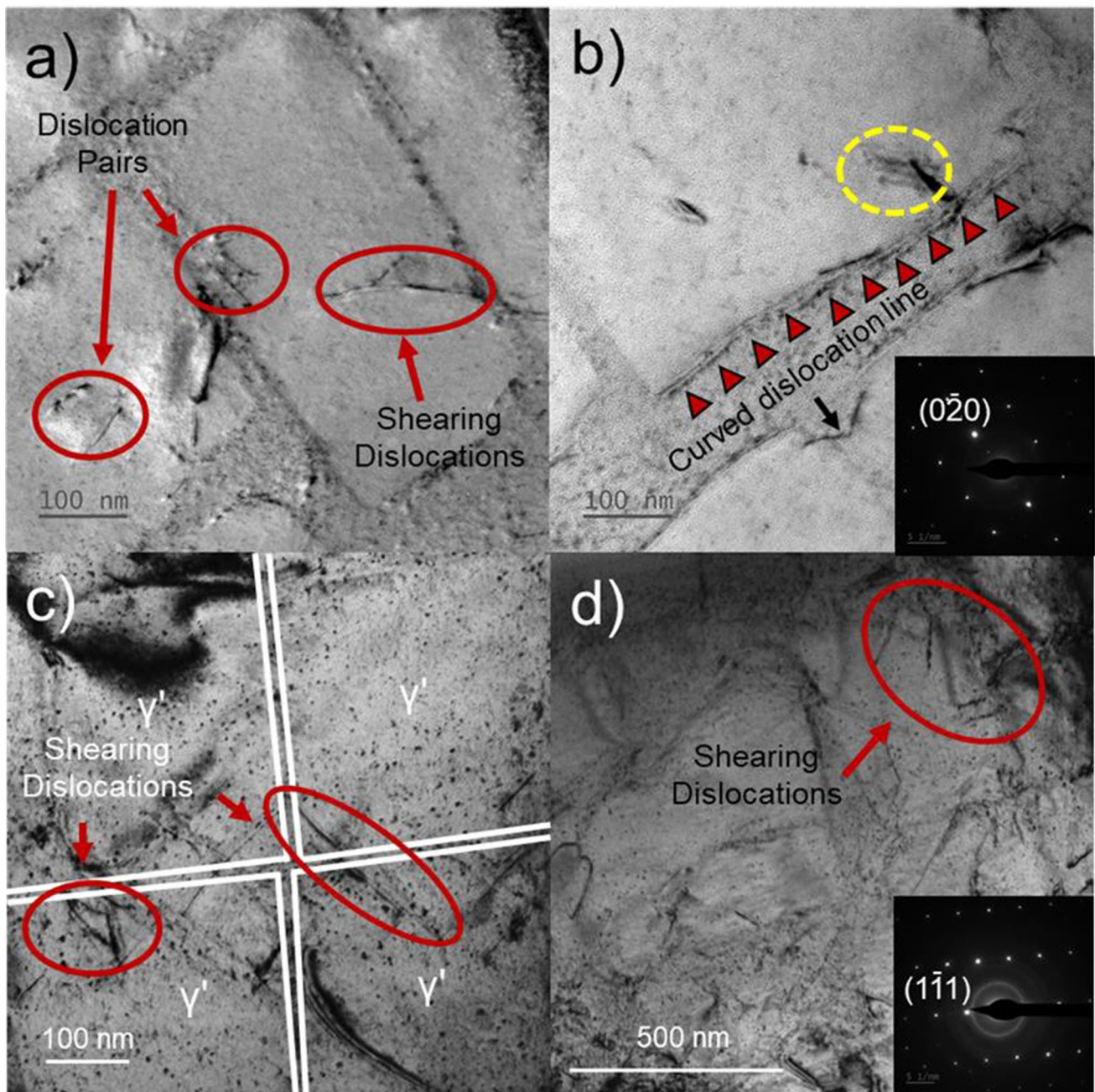
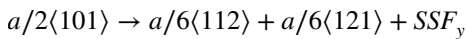


**Fig. 9** Bright field TEM images of a region 150  $\mu\text{m}$  from the sample surface following LP+TME both **a, b** prior to and **c, d** following thermal exposure with **a, c, d** evidence of  $\gamma'$  shearing, **b** SSFs marked by the yellow dashed circle, and **b** interfacial dislocations marked by

red triangles. SAED pattern for the pre-thermally exposed condition is shown in (b) while the pattern for the thermally exposed condition is shown in (d).  $\gamma'$  precipitates are outlined in (c) due to low contrast with the surrounding matrix

in a single-crystal Ni-based superalloy treated with 3 layers of laser peening at 7 GW/cm<sup>2</sup> along with glide and climb in the  $\gamma$  channels [9]. In addition, superlattice stacking fault (SSF) can be observed within the  $\gamma'$  precipitate in Fig. 9b.

According to previous studies [33–35], SSFs originate from the disassociation of an  $a/2 \langle 101 \rangle$  perfect dislocation in the following manner:



SSFs were not observed elsewhere within the region of interest used for the TEM study, and thus it cannot be said conclusively to what extent SSF shearing plays a role in plastic deformation. It is clear though that precipitate shearing is a primary mechanism near the LP+TME-treated surface. As was seen in the SEM images from Fig. 8, the  $\gamma/\gamma'$  microstructure following thermal exposure remained unchanged with the  $\gamma'$ , maintaining its coherency with the matrix (indicated by the sharp corners of the precipitates) as well as showing no obvious coarsening (Fig. 9c and 9d). Dislocations are again observed shearing through precipitates as well as congregating in the  $\gamma$  channels. Typically, interfacial dislocations aid in  $\gamma'$  coarsening at high temperatures [36], but under the thermal loads conducted in this work, the precipitates remained stable. Of course, at higher temperatures, this behaviour may change and will be investigated further in future work.

### 3.4 Residual stresses

Figures 10, 11, and 12 show plots of the residual eigenstresses in the laser-peened CMSX-4@ coupons determined

by the slitting method, before thermal exposure. Due to the single-crystal makeup of the test samples, it was not possible to use classical X-ray diffraction which more accurately measures near-surface stress. Because the slitting technique tends to report surface stresses greater than actual, it is expected that there is less near-surface stress than indicated by the figures and actually a hook-like shape to the eigenstress curves starting at about 500 mm depth and reducing the surface stress by about 200 MPa. The slitting technique is known to be accurate in measuring deeper stress, so there is confidence in measurements reported for the deeper depths out to and including 8 mm depth [26, 37, 38]. The large laser energy which enabled the large beam spot size used in this work is the primary reason for the deep levels of compressive plastic response and residual stress and thus favoured use of the deep measurement capability afforded by the crack compliance “slitting”. This approach is not needed for techniques such as shot peening and ultrasonic peening that generate relatively shallow plastic deformation. However, the deep plastic deformation generated by laser peening results in significant strain even in samples of 25 mm and 50 mm thicknesses. So in order to more correctly report strain at depth and not a combination of stress and strain, we use the eigenstress correction. Referring to the figures, in a slitting measurement the deepest (right hand) portion of the measurement results from the spherical strain induced in the given sample. Since the stiffness of the sample increases as the cube of the thickness, calculating and subtracting out this strain results in a stress value, the eigenstress, independent of the thickness of the measurement sample.

**Fig. 10** Effects of three different laser irradiances on the residual stress depth profile of CMSX-4@ laser-peened samples and SP sample. The insert plot adds the shot-peening result and shows a magnified view of the shallow shot-peening depth contrasting the deeper plastic penetration of the laser peening

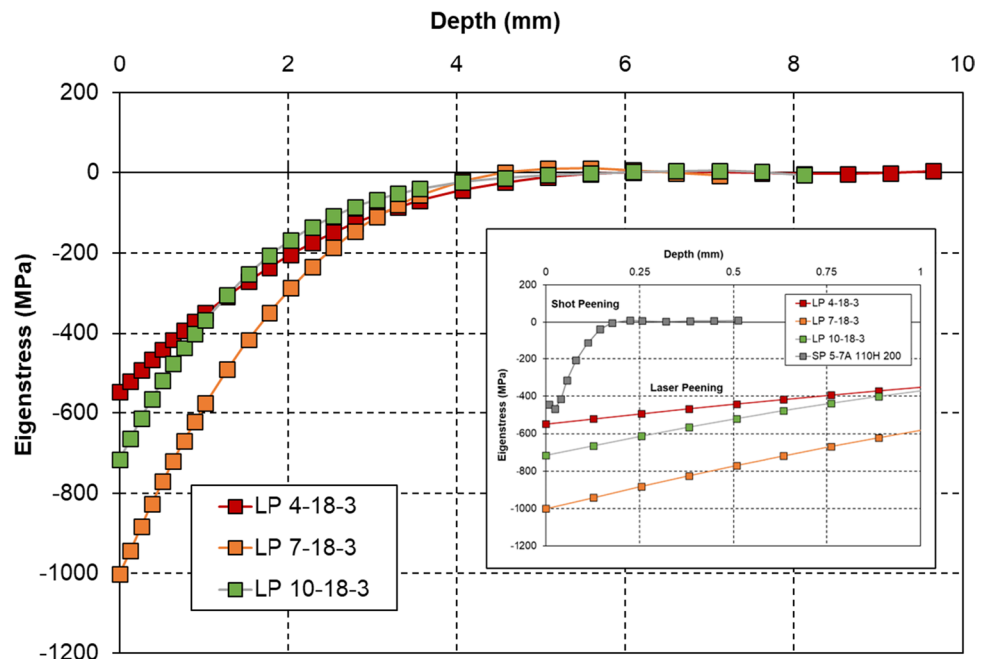


**Fig. 11** Effects of different laser passes on the residual stress (eigenstress) depth profile of CMSX-4 laser-peened samples

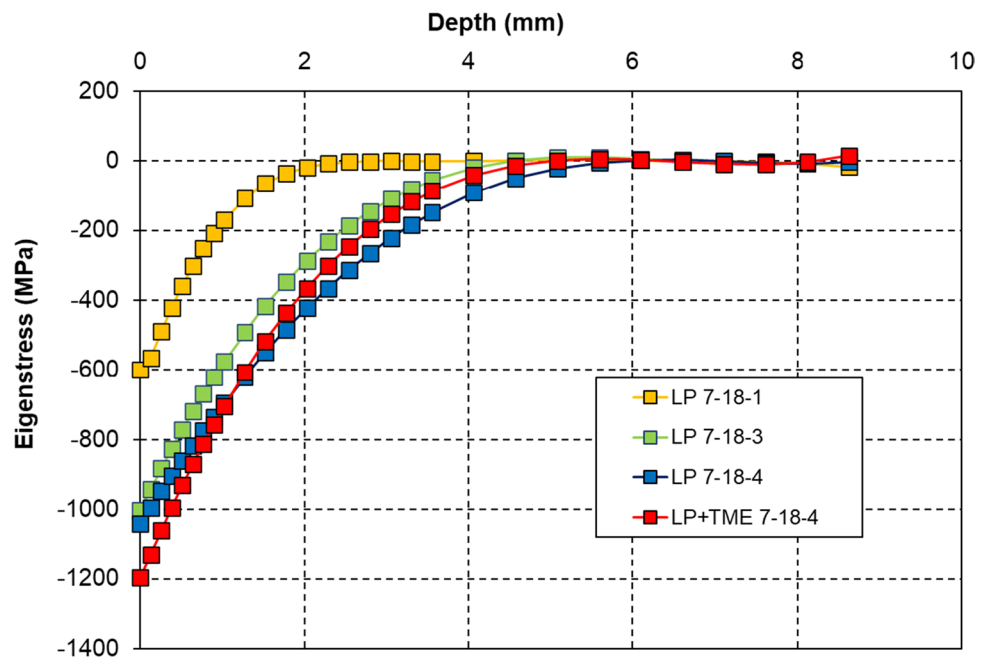
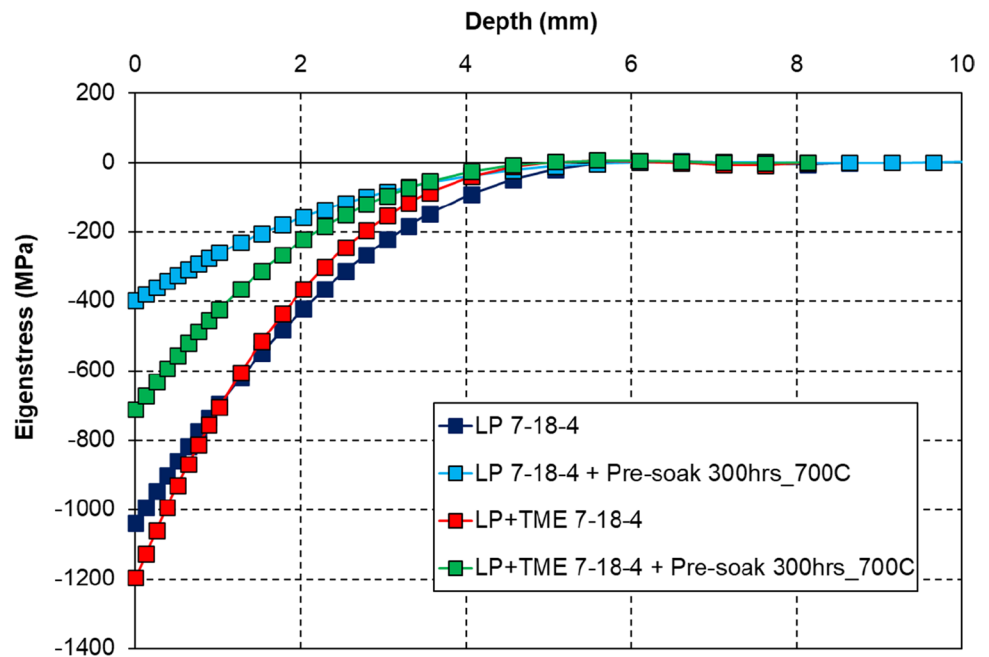


**Fig. 12** Eigenstress depth profile of CMSX-4 laser-peened specimens before and after thermal exposure at 700 °C for 300 h



The profiles in Fig. 10 show that residual eigenstress in the [100] direction penetrates to 5 mm depth, meaning that fully half the thickness of the block has been plastically strained. As a result, the top layer of the block elongates, resulting in a combination of residual stress and bending of the block. In comparison, equivalent peening of a block of greater thickness would result in less bending strain scaling by the cube of the thickness difference. This reduced transition to strain would result in greater measured residual stress. The eigenstress extrapolates the specimen thickness to infinity and determines the stress that would have occurred in a specimen that did not

strain. This laser-generated strain can then be applied analytically in a finite element program to a 3D model of the component giving accurate prediction of resulting stress and strain generated in that particular geometry. High-energy laser peening, such as used in this work, employs laser energy output in the range of 20 J/pulse [39]. The high energy enables the use of a relatively large spot size (0.35 to 1 cm<sup>2</sup>) while keeping the irradiance at the required high-power density needed to create sufficient pressure to plastically yield the material to the deeper depth. This can be contrasted to low-energy laser peening of 1 J/pulse or less [40] and the correspondingly smaller

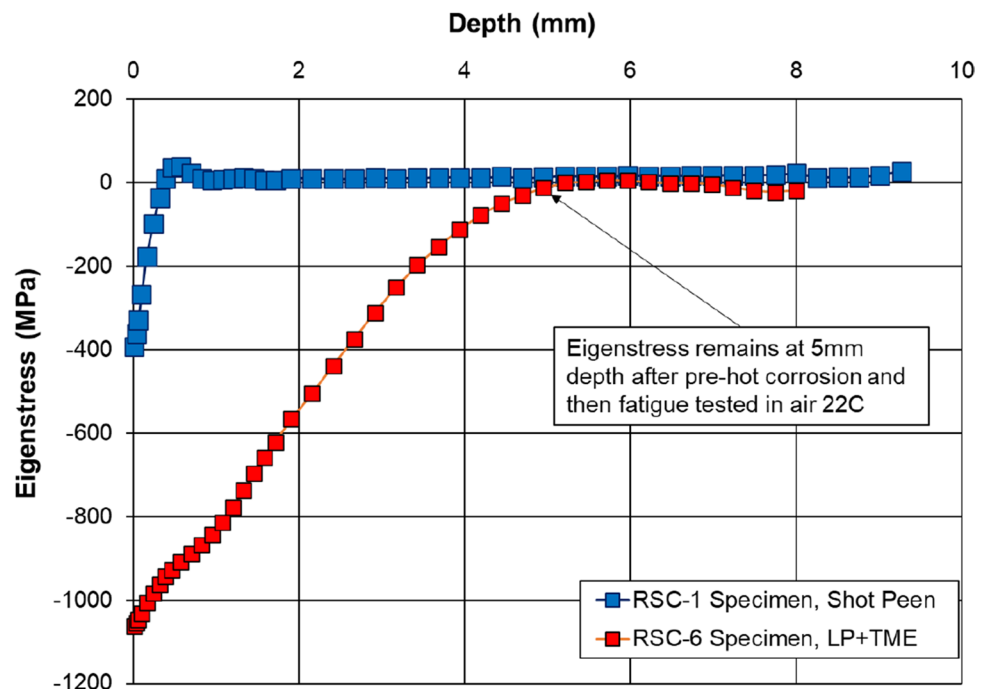
(0.05 cm<sup>2</sup>) footprint needed to keep the irradiance sufficiently high, in the 3 to 10 GW/cm<sup>2</sup> range, so as to produce a plastic response. The large spot size of the current work enables the pressure wave to deeply penetrate as a planar wave before geometrically rarefying and dropping below the useful plastic response value. These large spot sizes enable deep levels of plastic deformation that can reach up to 12 mm or more [41]. Deep levels of plastic deformation generate deep compressive stresses critically important to enhancing fatigue strength and preventing corrosion-initiated cracking.

Figure 11 shows the effect of laser treatment layers on the residual eigenstress depth profile generated in the single-crystal CMSX-4 prior to thermal soak and fatigue testing. The laser treatment employed 1, 3, 4 layers of peening with 100% coverage each layer. Additional treatment of 4 layers with annealing cycles at constant 7 GW/cm<sup>2</sup> was examined. The depth of compressive residual eigenstresses at the surface increased in the range of  $-564.82 \pm 82$  to  $-1196 \pm 16.6$  MPa as the laser treatment layers progressively increased from 1 laser pass (LP 7–18-1) to 4 laser passes with annealing cycles (LP+TME 7–18-4) conditions. This suggests that the depth of compressive residual stress increases with number of LP layers applied as expected, but also annealing cycles after each layer treated (up to 4 layers) increased the level of surface compressive residual stresses as well as providing good retention post-annealing cycles at 700 °C. Thus, it is important to highlight that it is possible to obtain higher compressive residual stresses beyond the surface as well as its retention through a combination of annealing cycles and higher number laser of passes. This approach has the additional advantage of obtaining higher dislocation networks.

The residual eigenstress profiles in Fig. 12 indicate that the stress relaxation following thermal exposure significantly reduced residual eigenstress depth profile on both LP 7–18-4 and LP+TME 7–18-4 conditions after 300 h at 700 °C from  $-1039$  to  $-399$  MPa and  $-1196$  to  $711$  MPa, respectively. Despite relaxation, the compressive eigenstress depths are similar to pre-thermal exposure, extending around 5.0 mm beneath the laser-treated surface, and the LP+TME processing shows superior stress retention near the surface. This is somewhat to be expected as the relaxation is a diffusion process propagating in from the surface. The time history of stress relaxation for times exceeding thousands of hours will be of importance for practical applications and a topic of further study.

The combined effects of thermal and cyclic loading can lead to complex stress relaxation [42–44]. Figure 13 shows the residual eigenstresses curves for both the SP (RSC-1) and an LP+TME (RSC-6) specimen after hot corrosion exposure and then fatigue testing. Compared to Fig. 10 where the measurements were performed before thermal exposure and fatigue testing, the SP curves show little loss of compressive eigenstress but do show the shallow 0.6 mm depth of plastic response. Comparing the LP+TME 7–18-4 eigenstress curve of Fig. 10 (before thermal exposure and fatigue testing) to the curve of Fig. 13, the all-important 5 mm depth of compressive eigenstress has been retained. Of interest, the Fig. 12 eigenstress measurement of the LP+TME specimen (after thermal exposure but before fatigue testing) shows a reduction of surface stress, whereas Fig. 13 shows this surface eigenstress retained after fatigue testing. Since the measurement of Fig. 10 was done by slitting and the geometry of the

**Fig. 13** Eigenstress in shot-peened and laser-peened fatigue specimens after peening, hot corrosion exposure, and then fatigue tested. Computed eigenstresses show the plastic strain induced by shot peening penetrated to a depth of about 0.6 mm, whereas the plastic strain of the laser peening penetrated and remained to a depth of 5 mm



specimens of Fig. 13 did not allow slitting and were thus done by hole drilling, there could be a technique error or the difference could or could be real and associated with strain hardening resulting from the 12 million cycles of fatigue testing that RSC-6 endured and stress loads above yield stress levels. Figures 10 and 13 do agree on the 5 mm depth of the penetration of the laser peening. Note that the eigenstress curve in a disc for the 7–18-3 process of Fig. 10 compares very closely to the eigenstress of RSC-6 of Fig. 13, a semi-circular fatigue specimen. This agreement is another confirmation of the geometry independence of the eigenstress method. These results suggest the importance of the deep level of eigenstress for good fatigue life and strength. The fatigue improvement observed in this work correlates directly with the depth of the eigenstress as the eigenstress in the SP specimen penetrated to only 0.6 mm, whereas in the laser-peened specimen it penetrated to 5 mm a difference greater than 8.

It should be also noted that the residual stresses generated by laser peening in the measurement samples were near the yield stress of the CMSX-4 material (940–1150 MPa), and thus elastic–plastic response can generate stress measurement errors. In his review and analysis of plasticity effects in slitting measurements [45], a detailed analysis and computations were defined for quantifying the errors generated by plasticity in performing slitting measurements. The most significant issue is when the residual stress in the measured sample is near the yield stress of the material, as is the case for the laser-peened samples of this study. Errors are largest near the surface and become smaller as measurements are taken at deeper depths. On the positive side for this work, samples with larger thickness-to-width ratio have lower plasticity errors compared to thin samples, as is the case for the disc samples used in this work with thickness to diameter ratio of  $10\text{ mm}/23\text{ mm}=0.43$ . It is recognised that in this work plasticity errors would be present in the analysis, especially near the surface, but the primary intent of the measurements was to choose a laser irradiance that would provide deep eigenstress to enable good fatigue and corrosion-fatigue performance with minor straining of the fatigue specimen; subsequent testing showed the chosen irradiance of  $7\text{ GW}/\text{cm}^2$  for peening spot illuminations did provide good fatigue performance although a different irradiance could be more optimum in a different geometry. It is recognised that slitting measurement error maximises near the surface and results from the first 0.25 mm should best be neglected [45]. For the current work, the mean error, deviation in fit of the data to the model, is about 9 MPa and the maximum error is 22 MPa. The error in determining the depth of compressive stress is about 5% in the important 5-mm-depth region. Although not done to date, the analysis by [45] could in the future be applied to the slitting strain measurements obtained in this work to generate the plasticity corrections to more accurately determine the stress profiles generated by the various laser-peening parameters.

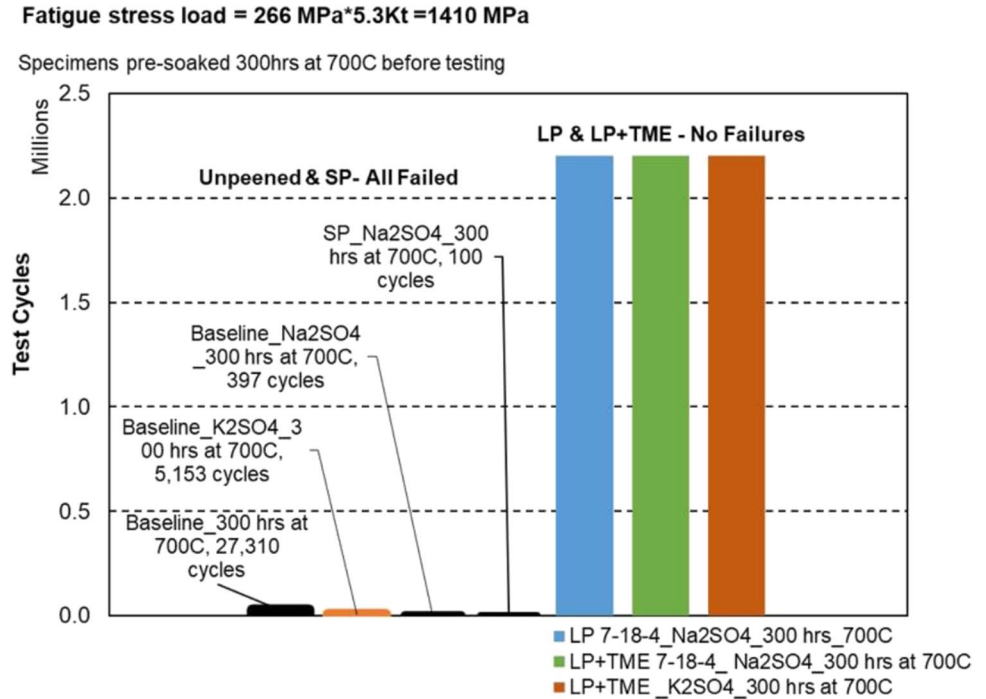
### 3.5 Fatigue life and strength

All specimens were initially tested at 4.817 kN (231 MPa) load, and when reaching or exceeding runout were uploaded to 5.538 kN (266 MPa) and further cycled until failure or runout. Subsequently, the three laser-peened specimens that did not fail were further tested by increasing their load by another 15%, testing to approximately 2 million cycles or 10% displacement compliance and again uploading and testing until runout or failure occurred. Typically, in polycrystalline material fatigue specimens progress from first observation of a small visible crack to full compliance failure after only a few hundred additional fatigue cycles. In contrast, for the single-crystal material, large cracking would be clearly visible, yet specimens continued to operate for thousands of cycles without reaching the 10% increased displacement limit. However, cracked specimens failed near immediately upon uploading of 15%. This was the case for the non-laser-peened specimens, that is the baseline and shot-peened pre-hot corrosion exposed specimens (see Fig. 14).

Figure 14 (and Table 6 in Appendix) shows fatigue life test results for the eight single-crystal specimens available and tested. Although a limited availability of bars prevented fabricating the large specimen count needed for statistically significant testing, the consistent large fatigue life improvement of the three laser-peened specimens compared to the four non-peened and one shot-peened specimen strongly suggests the large benefit observed from the laser peening is real. All three LP and LP+TME specimens hot corrosion exposed after peening showed no hint of fatigue failure during the 266 MPa loading and continued uncracked throughout the 2.2 million cycle test to runout. The statistics of all three laser-peened specimens attaining two million cycles and then million cycle runouts at higher stress loading without evidence of cracking and all non-laser-peened pre-hot corrosion exposed specimens failing after substantially fewer cycles at lower loading. The non-laser-peened specimens showed easily visible cracks at the 231 MPa loading but did not reach the 10% compliance. Once uploaded to 266 MPa with relatively large, easily visible cracks apparent, these specimens reached displacement failure within 27,000 or fewer cycles and thus could be considered a failure at the lower 231 MPa level where the large cracking developed. For reporting purposes, failure was defined as when the specimens developed clearly visible cracks.

The runout experienced at 266 MPa loading for the LP and LP+TME specimens enabled uploading and consequent evaluation of fatigue strength. Figure 15 shows the fatigue strength test results where after runout at 266 MPa, the three unfailed specimens were uploaded by 15% in stress and further tested. After achieving runout at this increased loading and with no visible cracking or displacement failure, the three LP specimens were yet further uploaded and tested. Each time runout was achieved, specimens were again uploaded by an additional 15% and tested to runout or until failure did occur. Eventually, the LP specimen failed at 413 MPa applied loading, a loading

**Fig. 14** Fatigue life of notched four-point bending CMSX-4 nickel-based superalloy specimens left unpeened or treated by shot or laser peening then with pre-test thermal or chemical-plus-thermal exposure and finally fatigue tested as noted

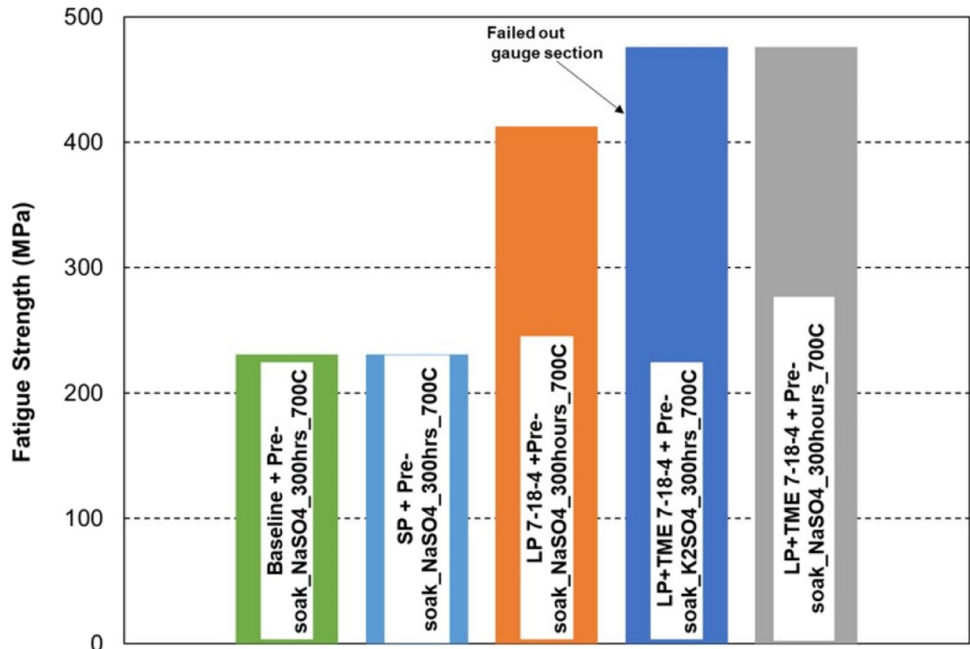


representing 80% increase in fatigue strength over the 231 MPa non-LP failures. The LP + TME specimens eventually tested to a fatigue strength of 476 MPa with one of the LP + TME specimens failing after 1.5 million cycles, a 100% fatigue strength increases. However, the other LP + TME specimen failed outside the gauge and could thereby only be classified as non-failed at this highest stress level.

Overall, the results for both standard high-energy laser peening and the same processing with the added cyclic annealing

(LP + TME) both give improved performance of the single-crystal material after pre-corrosion exposure at high temperature and then fatigue testing at room temperature. However, the interspersed process appears to be the better. Both laser-peening results contrast in our tests to the significantly diminished performance clearly observed from untreated and shot-peened (shallow depth of compressive stress) specimens. The large footprint enabled by the high-energy approach to laser peening uniquely enables deep penetration of a plastic

**Fig. 15** Fatigue strength test results for CMSX-4 specimens. Specimens were unpeened or peened as noted, then coated with sodium sulphate, and exposed for 300 h at 700 °C before finally fatigue testing at room temperature



pressure wave above the material's plastic limit and thereby generates the deepest level of compressive residual stress. The cyclic thermal annealing additionally appears to help lock in the deep residual stress and further benefit performance. This deep compressive residual stress and thermal stability support the enhanced fatigue test results and appear to explain the superior corrosion-fatigue performance of the laser process. Additional studies will focus on optimising the number of thermal and annealing cycles in the LP + TME process while attaining better understanding of mechanisms, enabling the corrosion-fatigue strength and lifetime enhancements. Importantly, future studies will extend evaluations to longer duration and higher temperature exposures.

### 3.6 Fracture surface analysis

Fracture surfaces of the failed specimens were examined with optical microscopy and are presented in Fig. 16 for all four cases. As can be seen from Fig. 16a, the fracture face of the unpeened pre-hot corrosion exposed fatigue specimen is dominated by long cleavages in stepwise ridge patterns perpendicular to the load direction, suggesting faster crack growth until the final fracture in the absence of peening. Cleavage and ridge facets were also observed in the shot-peened specimen along with secondary cracks perpendicular to the crystallographic slip direction, as shown in Fig. 16b. This implies obvious weakening of the  $\gamma/\gamma'$  precipitates-strengthening mechanism and occurrence of residual tensile stresses. Both unpeened and shot-peened specimen failures were dominated by accelerated crack growth due to tensile overload after a stress load increment.

In contrast, fractured cross-sections of laser peened specimens show complex fracture facets with beach-type striations along crystallographic planes and clear evidence of slower crack growth features are evident even after stress load increments (Fig. 16c and 16d). The fracture faces of laser-peened specimens showed improved fatigue resistance properties in CMSX-4 superalloy which is attributed to the effect of LP generating deep compressive residual stresses. However, if we examine the fracture surface of LP and LP + TME pre-hot corrosion exposed fatigue specimens, the fracture facets are entirely different. There is substantial spacing between fatigue striation steps on fracture cross-section of LP + TME (Fig. 17b) compared to fine and hairline-type striations observed in LP-fractured specimen (Fig. 17a). After laser-peening treatment, compressive residual stresses and dislocation slips act as a mechanism of crack growth retardation, limiting the crack extension along slip planes and delaying the failure occurrence, thus improving the overall life of laser-peened alloys. So the inhibitory effects on crack growth from the laser peening treatment can be mainly attributed to the high levels of compressive residual stresses introduced during high-energy peening with interspersed annealing cycles.

Typically, stress corrosion and fatigue crack mechanisms are characterised by three stages, viz., incubation and crack

nucleation, crack growth, and final fracture or overload [46]. In this study, slitted notch areas in all fatigued specimens are representative of stress raiser areas and crack nucleation. The cross-section of the slitted notch area of the SP specimen in Fig. 16a shows evidence of surface deterioration caused by the corrosion attack during pre-hot corrosion exposure. Pits and surface depletion were also observed, as shown in Fig. 18a. Although SP treatment introduces compressive stresses, it also facilitates inward diffusion of corrosive elements to the substrate due to poor surface roughness, and this acts as a localised stress concentration. As a result, the SP greatly reduces resistance to cracking and corrosion due to poor surface roughness. On the other hand, as shown in Fig. 18b, fracture morphology of the slitted notch area of an LP + TME specimen shows no signs of corrosion pitting and surface depletion. The lack of degradation due to corrosion combined with the much deeper residual stress of the laser peening enables the much improved fatigue performance.

It is important to mention that corrosion behaviour in single-crystal nickel-based superalloys is strongly affected by its  $\gamma/\gamma'$  phases and the mechanical properties of its surface and near-surface layers [18]. After laser-peening treatment, the presence of a surface strain-hardening layer, a network of high-density dislocations, and compressive residual stresses (CRS) are key mechanisms of corrosion and fatigue resistance in metals. In an SC nickel-based superalloy, high dislocation density in  $\gamma/\gamma'$  phases can create a stable outward diffusion of corrosion-resistant elements such as chromium and aluminium in  $\gamma/\gamma'$  phases, respectively [12, 13]. This outward diffusion promotes formation of a dense and homogenous protective oxide layer that suppresses the diffusion of corrosive elements into the superalloy substrate including sulphur, chlorine, sodium, etc. As result, laser peening significantly reduces the corrosion attack and crack nucleation. In addition, the surface strain-hardening layer and CRS induced by laser peening aid strong adhesion between the protective oxide layer and the substrate as well as retarding the crack growth. Moreover, it was demonstrated that the new cyclic laser peening plus interspersed annealing (LP + TME) treatment provided excellent thermal stability and good retention of CRS under pre-corrosion thermal conditions and thereby led to increased fatigue cycles. Therefore, laser-peening treatment can be applied to alloys to improve resistance to high-temperature corrosion and fatigue.

## 4 Conclusions

This study focussed on the relaxation of residual stresses and fatigue strength post hot-corrosion exposure of single-crystal nickel CMSX-4® superalloy by shot peening, laser peening, and cyclic laser peening plus annealing (LP + TME). The following conclusions are drawn from the present study:

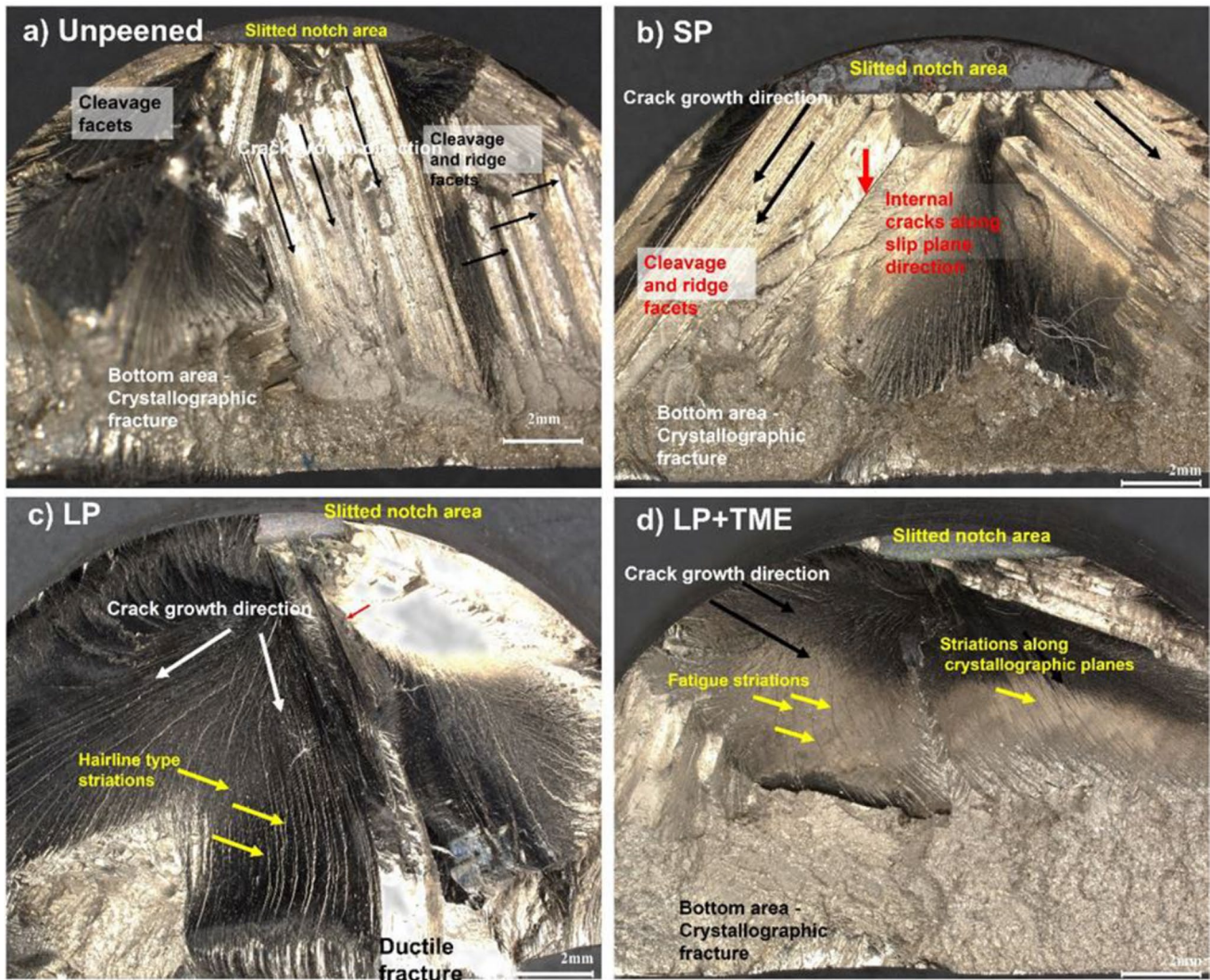


**Fig. 16** Fracture faces of pre-corrosion and thermally soaked fatigue specimens. Microscopy images: **a** unpeened specimen, **b** shot peened, **c** laser peened, and **d** cyclic laser peened with interspersed annealing (LP+TME)

- The surface roughness of the LP-treated specimens increases upon peening with increasing power density, from 4 to 10 GW/cm<sup>2</sup>. Additionally, upon thermal exposure, the surface of the LP specimens became less rough.
- Taken in aggregate, the fatigue tests represent five test results for specimens that were not laser peened vs. three laser-peened specimens. All non-laser-peened specimens failed after a short number of cycles and all laser-peened specimens exhibited greater than 80 times longer life as none of the laser-peened specimens failed until loaded by a factor of almost 2 in the stress load. This constitutes relatively convincing initial test statistics that the deep stress of the laser peening was retained after the pre-hot corrosion exposure to 700 °C for 300 h, yet resulted in the significant fatigue strength and lifetime improvement of the laser-peened single-crystal CMSX-4 specimens under conditions tested. Limited availability of single-crystal boules of CMSX-4 prevented more extensive testing. Future testing is planned using the next-generation CMSX-4 plus material.
- After high-energy LP and LP + TME treatment, morphology of the  $\gamma/\gamma'$  precipitates remains unchanged, not degrading the pre-existing strengthening mechanism. After pre-exposure under sulphate corrosives and high-temperature (300 h at 700 °C), the precipitates remain stable. The  $\gamma/\gamma'$  interfacial dislocations, curved dislocations lines, and dislocation shearing of the  $\gamma'$  phases observed contributed to thermal stability of LP + TME specimens under conditions tested. This yields higher retention of the hardened layer and compressive residual stresses than after shot peening.

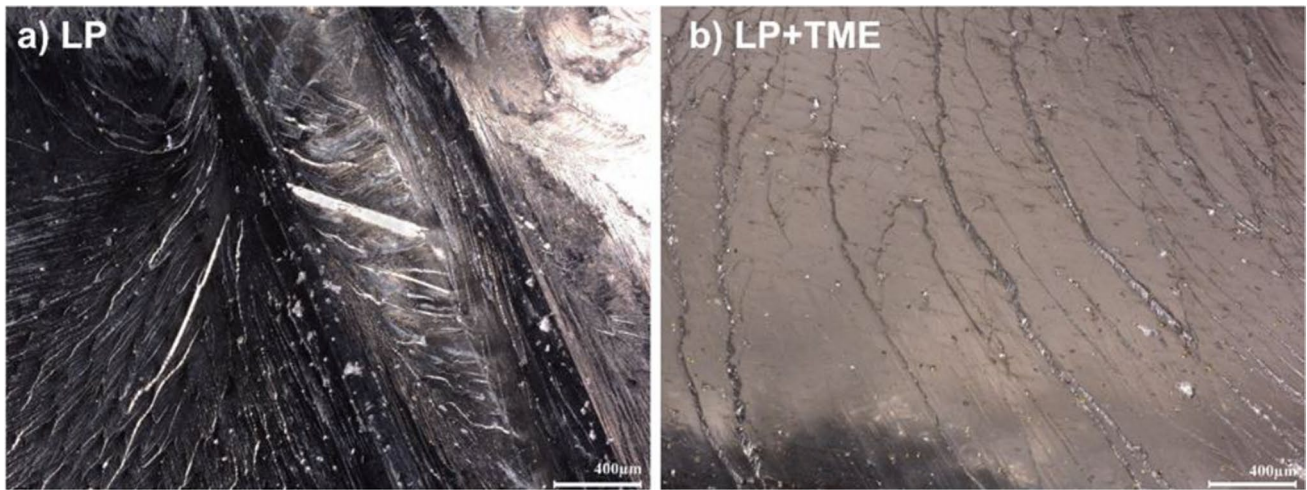


**Fig. 17** Micrographs of fracture surface of **a** LP and **b** LP+TME specimens showing fatigue striation on fracture cross-sections at higher magnification

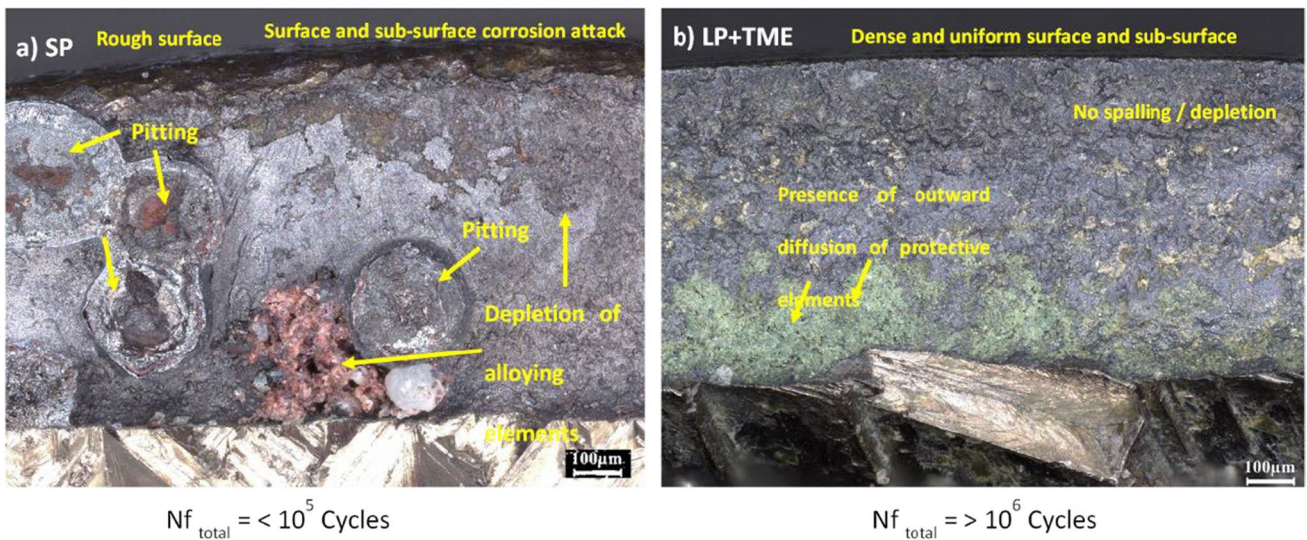


**Fig. 18** Micrographs of fatigue notch fracture faces: **a** SP specimen and **b** LP+TME specimen

- With respect to residual stresses, the high-energy laser peening enabled a large spot size of 12 mm<sup>2</sup> with 7 GW/cm<sup>2</sup> and thereby introduced deeper compressive eigenstresses up to a range of 4 to 5 mm. The accumulation of annealing cycles and high number of laser passes facilitated generation of high dislocation networks. This contributed to stable retention of compressive eigenstresses post thermal exposure and mechanical fatigue loading under the conditions tested.
- Pits and surface depletion are observed on the fracture surfaces of slitted notches of the SP specimen after hot corrosion exposure and post fatigue testing. While on LP+TME there were no signs of severe corrosion pits and surface depletion. The presence of high surface hard-

ening, deeper compressive residual stresses, and a high dislocation network are the key mechanisms of corrosion and fatigue resistance. These microstructure characteristics generated by LP+TME prevented inward diffusion of corrosive species and facilitates outward diffusion of protective elements including chromium and aluminium in  $\gamma/\gamma'$  phases, respectively.

- Deeper compressive eigenstresses by high-energy laser peening plus interspersed annealing (LP+TME) effectively reduced the notch mean stress and restrained the propagation of the crack, thereby improving fatigue strength. Fatigue strength of laser peened specimens improved by 2:1 or more beyond the counterpart unpeened and shot-peened specimens under the conditions tested.

## Appendix

**Table 6** Summary of fatigue test results

| SN    | Process  | Stress (MPa) | *5.3Kt (MPa) | Life cycles | Failure | Remarks      |
|-------|--|--------------|--------------|-------------|---------|--------------|
| RSC-1 | SP_Na <sub>2</sub> SO <sub>4</sub> _300 h at 700C            | 231          | 1224.3       | 379,101     | No      |              |
|       |  | 266          | 1409.8       | 100         | Yes     |              |
| RSC-2 | Baseline_300 h at 700C                                       | 231          | 1224.3       | 2,075,840   | No      |              |
|       |  | 266          | 1409.8       | 27,310      | Yes     |              |
| RSC-3 | LP 7–18-4_Na <sub>2</sub> SO <sub>4</sub> _300 hrs_700C      | 266          | 1409.8       | 2,156,128   | No      |              |
|       |  | 308          | 1632.4       | 2,225,237   | No      |              |
|       |  | 357          | 1892.1       | 2,259,301   | No      |              |
|       |  | 413          | 2188.9       | 1,659,157   | Yes     |              |
| RSC-4 | LP+TME 7–18-4_Na <sub>2</sub> SO <sub>4</sub> _300 h at 700C | 266          | 1409.8       | 2,232,529   | No      |              |
|       |  | 308          | 1632.4       | 2,268,573   | No      |              |
|       |  | 357          | 1892.1       | 2,517,277   | No      |              |
|       |  | 413          | 2188.9       | 2,037,810   | No      |              |
| RSC-5 | Baseline_K <sub>2</sub> SO <sub>4</sub> _300 h at 700C       | 231          | 1224.3       | 1,171,667   | No      |              |
|       |  | 266          | 1409.8       | 5,153       | Yes     |              |
| RSC-6 | LP+TME_K <sub>2</sub> SO <sub>4</sub> _300 h at 700C         | 231          | 1224.3       | 1,118,901   | No      |              |
|       |  | 266          | 1409.8       | 2,901,727   | No      |              |
|       |  | 308          | 1632.4       | 2,654,241   | No      |              |
|       |  | 357          | 1892.1       | 3,441,991   | No      |              |
| RSC-7 | Baseline_Na <sub>2</sub> SO <sub>4</sub> _300 h at 700C      | 413          | 2188.9       | 82,006      | Yes     | out of gauge |
|       |  | 231          | 1409.8       | 397         | Yes     |              |
| RSC-8 | Baseline   | 231          | 1224.3       | 670,002     | No      |              |
|       |  | 266          | 1409.8       | 175,517     | Yes     |              |

**Author contribution** All authors contributed to the study conception and design. Conceptualisation, investigation, material preparation, data collection, and analysis performed by Nicolau Morar and Llyod Hackel. Analytical microscopy by Noah Holtham; residual stress measurements by Montu Sharma and Adrian DeWald; supervision and review by Keivan Davami and Rajkumar Roy. The first draft of the manuscript was written and edited by Nicolau Morar and all authors commented on previous versions of the manuscript. All authors read and approved the final manuscript.

**Funding** The authors acknowledge the support of the Engineering and Physical Research Council (EPSRC) Platform Grant (grant number EP/P027121/1).

### Declarations

**Ethical approval** This work does not contain any ethical issues or personal information.

**Consent to participate** No human or animal was involved in this work; thus, no consent was required.

**Consent for publication** All authors have given their permission for publishing this work.

**Competing interests** The authors declare no competing interests.

**Open Access** This article is licensed under a Creative Commons Attribution 4.0 International License, which permits use, sharing, adaptation, distribution and reproduction in any medium or format, as long as you give appropriate credit to the original author(s) and the source, provide a link to the Creative Commons licence, and indicate if changes were made. The images or other third party material in this article are included in the article's Creative Commons licence, unless indicated otherwise in a credit line to the material. If material is not included in the article's Creative Commons licence and your intended use is not permitted by statutory regulation or exceeds the permitted use, you will need to obtain permission directly from the copyright holder. To view a copy of this licence, visit <http://creativecommons.org/licenses/by/4.0/>.

### References

1. Fullagar KPL, Broomfield RW, Hulands M et al (1996) Aero engine test experience with CMSX-4® alloy single-crystal turbine blades. *J Eng Gas Turbine Power* 118:380–388. <https://doi.org/10.1115/1.2816600>
2. Kobayashi M, Matsui T, Murakami Y (1998) Mechanism of creation of compressive residual stress by shot peening. *Int J Fatigue* 20:351–357. [https://doi.org/10.1016/S0142-1123\(98\)00002-4](https://doi.org/10.1016/S0142-1123(98)00002-4)

3. Sano Y, Akita K, Masaki K, et al (2006) Laser peening without coating as a surface enhancement technology. *JLMN-J Laser Micro/Nanoeng* 1. <https://doi.org/10.2961/jlmn.2006.03.0002>
4. Hackel L, Rankin J, Racanelia T et al (2015) Laser peening to improve fatigue strength and lifetime of critical components I. *Procedia Eng* 133:545–555. <https://doi.org/10.1016/j.proeng.2015.12.677>
5. Hu X, Yang Y, Zhao J et al (2021) Surface integrity evolution of a Ni-based single crystal superalloy by laser shock peening. *Appl Surf Sci Adv* 6:100183. <https://doi.org/10.1016/j.apsadv.2021.100183>
6. Sihai L, Xiangfan N, Liucheng Z et al (2017) Thermal stability of surface nanostructure produced by laser shock peening in a Ni-based superalloy. *Surf Coat Technol* 311:337–343. <https://doi.org/10.1016/j.surfcoat.2017.01.031>
7. Lu GX, Liu JD, Qiao HC et al (2017) Surface nano-hardness and microstructure of a single crystal nickel base superalloy after laser shock peening. *Opt Laser Technol* 91:116–119. <https://doi.org/10.1016/j.optlastec.2016.12.032>
8. Cao J, Cao X, Jiang B et al (2021) Microstructural evolution in the cross section of Ni-based superalloy induced by high power laser shock processing. *Opt Laser Technol* 141:107127. <https://doi.org/10.1016/j.optlastec.2021.107127>
9. Geng Y, Dong X, Wang K et al (2020) Evolutions of microstructure, phase, microhardness, and residual stress of multiple laser shock peened Ni-based single crystal superalloy after short-term thermal exposure. *Opt Laser Technol* 123:105917. <https://doi.org/10.1016/j.optlastec.2019.105917>
10. Lu GX, Liu JD, Qiao HC et al (2017) Surface topography evolution of Ni-based single crystal superalloy under laser shock: formation of the nano-scale surface reliefs. *Appl Phys A* 123:213. <https://doi.org/10.1007/s00339-017-0814-8>
11. Tang Z, Wang K, Geng Y et al (2021) An investigation of the effect of warm laser shock peening on the surface modifications of [001]-oriented DD6 superalloy. *Int J Adv Manuf Technol* 113:1973–1988. <https://doi.org/10.1007/s00170-021-06763-7>
12. Geng Y, Mo Y, Zheng H et al (2021) Effect of laser shock peening on the hot corrosion behavior of Ni-based single-crystal superalloy at 750°C. *Corros Sci* 185:109419. <https://doi.org/10.1016/j.corsci.2021.109419>
13. Tang Z, Dong X, Geng Y et al (2022) The effect of warm laser shock peening on the thermal stability of compressive residual stress and the hot corrosion resistance of Ni-based single-crystal superalloy. *Opt Laser Technol* 146:107556. <https://doi.org/10.1016/j.optlastec.2021.107556>
14. Lu GX, Liu JD, Qiao HC et al (2017) Crack appearance of a laser shock-treated single crystal nickel-base superalloy after isothermal fatigue failure. *Surf Coat Technol* 321:74–80. <https://doi.org/10.1016/j.surfcoat.2017.04.044>
15. Tang Z, Wang K, Dong X et al (2021) Effect of warm laser shock peening on the low-cycle fatigue behavior of DD6 nickel-based single-crystal superalloy. *J Mater Eng Perform* 30:2930–2939. <https://doi.org/10.1007/s11665-021-05508-7>
16. Cockings H (2022) High temperature corrosion. In: Caballero FG (ed) *Encyclopedia of materials: metals and alloys*. Elsevier, Oxford, pp 464–475
17. Eliaz N, Shemesh G, Latanision RM (2002) Hot corrosion in gas turbine components. *Eng Fail Anal* 9:31–43. [https://doi.org/10.1016/S1350-6307\(00\)00035-2](https://doi.org/10.1016/S1350-6307(00)00035-2)
18. Ye C, Liao Y, Cheng G (2010) Warm laser shock peening driven nanostructures and their effects on fatigue performance in aluminum alloy 6160. *Adv Eng Mater* 12:291–297. <https://doi.org/10.1002/adem.200900290>
19. Rozmus-Górnikowska M, Kusiński J, Cieniek Ł, Morgiel J (2021) The Microstructure and properties of laser shock peened CMSX4 superalloy. *Metall Mater Trans A* 52:2845–2858. <https://doi.org/10.1007/s11661-021-06277-7>
20. Munther M, Rowe RA, Sharma M et al (2020) Thermal stabilization of additively manufactured superalloys through defect engineering and precipitate interactions. *Mater Sci Eng: A* 798:140119. <https://doi.org/10.1016/j.msea.2020.140119>
21. Hackel L, Fuhr J, Sharma M et al (2019) Test results for wrought and AM In718 treated by shot peening and laser peening plus thermal microstructure engineering. *Procedia Struct Integr* 19:452–462. <https://doi.org/10.1016/j.prostr.2019.12.049>
22. Liao Y, Suslov S, Ye C, Cheng GJ (2012) The mechanisms of thermal engineered laser shock peening for enhanced fatigue performance. *Acta Mater* 60:4997–5009. <https://doi.org/10.1016/j.actamat.2012.06.024>
23. Munther M, Tajyar A, Holtham N et al (2022) An investigation into the mechanistic origin of thermal stability in thermal-microstructural-engineered additively manufactured Inconel 718. *Vacuum* 199:110971. <https://doi.org/10.1016/j.vacuum.2022.110971>
24. Sengupta A, Putatunda S, Bartosiewicz L et al (1994) Tensile behavior of a new single-crystal nickel-based superalloy (CMSX-4) at room and elevated temperatures. *J Mater Eng Perform* 3:73–81. <https://doi.org/10.1007/BF02654502>
25. Walter D, Pilkey DFPZB (2020) Peterson's stress concentration factors, 4th edn. Wiley and Sons publisher
26. Hackel L, Rankin JR, Rubenchik A et al (2018) Laser peening: a tool for additive manufacturing post-processing. *Addit Manuf* 24:67–75. <https://doi.org/10.1016/j.addma.2018.09.013>
27. Hill MR, Dewald AT, Rankin JE, Lee MJ (2005) Measurement of laser peening residual stresses. *Mater Sci Technol* 21:3–9. <https://doi.org/10.1179/174328405X14083>
28. Achintha M, Nowell D (2011) Eigenstrain modelling of residual stresses generated by laser shock peening. *J Mater Process Technol* 211:1091–1101. <https://doi.org/10.1016/j.jmatprotec.2011.01.011>
29. Hill M, Lin W-Y (2002) Residual stress measurement in a ceramic-metallic graded material. *J Eng Mater Technol-Trans Asme - J Eng Mater Technol* 124. <https://doi.org/10.1115/1.1446073>
30. Rankin JE, Hill MR, Hackel LA (2003) The effects of process variations on residual stress in laser peened 7049 T73 aluminum alloy. *Mater Sci Eng, A* 349:279–291. [https://doi.org/10.1016/S0921-5093\(02\)00811-0](https://doi.org/10.1016/S0921-5093(02)00811-0)
31. Achintha M, Nowell D, Shapiro K, Withers PJ (2013) Eigenstrain modelling of residual stress generated by arrays of laser shock peening shots and determination of the complete stress field using limited strain measurements. *Surf Coat Technol* 216:68–77. <https://doi.org/10.1016/j.surfcoat.2012.11.027>
32. Peyre P, Fabbro R, Merrien P, Lieurade HP (1996) Laser shock processing of aluminium alloys. Application to high cycle fatigue behaviour. *Mater Sci Eng, A* 210:102–113. [https://doi.org/10.1016/0921-5093\(95\)10084-9](https://doi.org/10.1016/0921-5093(95)10084-9)
33. Wang GL, Liu JL, Liu JD et al (2017) Temperature dependence of tensile behavior and deformation microstructure of a Re-containing Ni-base single crystal superalloy. *Mater Des* 130:131–139. <https://doi.org/10.1016/j.matdes.2017.05.014>
34. Zhang H, Wang Q, Gong X et al (2021) Dependence on temperature of compression behavior and deformation mechanisms of nickel-based single crystal CMSX-4. *J Alloys Compd* 866:158878. <https://doi.org/10.1016/j.jallcom.2021.158878>
35. Milligan W, Antolovich S (1991) The mechanisms and temperature dependence of superlattice stacking fault formation in the single-crystal superalloy PWA 1480. *Metall Trans A* 22. <https://doi.org/10.1007/BF02664997>
36. He J, Cao L, Makineni SK et al (2021) Effect of interface dislocations on mass flow during high temperature and low stress creep of single crystal Ni-base superalloys. *Scr Mater* 191:23–28. <https://doi.org/10.1016/j.scriptamat.2020.09.016>

37. Vaidyanathan S, Finnie I (1971) Determination of residual stresses from stress intensity factor measurements. *J Basic Eng* 93:242. <https://doi.org/10.1115/1.3425220>
38. Alamos L, Prime M (1999) Residual stress measurement by successive extension of a slot: the crack compliance method. *Appl Mech Rev* 52:75–96. <https://doi.org/10.1115/1.3098926>
39. Dane C, Hackel L, Daly J, Harrison J (1998) Shot peening with lasers. *Adv Mater Processes* 153:37–38
40. Sano Y, Mukai N, Okazaki K, Obata M (1997) Residual stress improvement in metal surface by underwater laser irradiation. *Nucl Instrum Methods Phys Res B* 121:432–436. [https://doi.org/10.1016/S0168-583X\(96\)00551-4](https://doi.org/10.1016/S0168-583X(96)00551-4)
41. DeWald AT (2005) Measurement and modeling of laser peening residual stresses in geometrically complex specimens. University of California, Davis
42. Evans A, Kim S-B, Shackleton J et al (2005) Relaxation of residual stress in shot peened Udimet 720Li under high temperature isothermal fatigue. *Int J Fatigue* 27:1530–1534. <https://doi.org/10.1016/j.ijfatigue.2005.07.027>
43. Foss BJ, Gray S, Hardy MC et al (2013) Analysis of shot-peening and residual stress relaxation in the nickel-based superalloy RR1000. *Acta Mater* 61:2548–2559. <https://doi.org/10.1016/j.actamat.2013.01.031>
44. Zhou W, Ren X, Ren Y, et al (2017) Laser shock processing on Ni-based superalloy K417 and its effect on thermal relaxation of residual stress. *Int J Adv Manuf Technol* 88. <https://doi.org/10.1007/s00170-016-8796-9>
45. Prime MB (2010) Plasticity effects in incremental slitting measurement of residual stresses. *Eng Fract Mech* 77:1552–1566. <https://doi.org/10.1016/j.engfracmech.2010.04.031>
46. Brooking L, Sumner J, Gray S, Simms NJ (2017) Stress corrosion of Ni-based superalloys. *Mater High Temp* 35:1–10. <https://doi.org/10.1080/09603409.2017.1392414>

**Publisher's note** Springer Nature remains neutral with regard to jurisdictional claims in published maps and institutional affiliations.